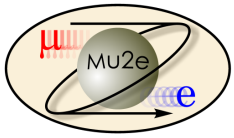

Study of the kinetics of the Undoped CsI Emission

Riccardo Rigano
Universita' degli Studi Roma Tre

Supervisor: Pasha Murat
Summer student 2015

September 25, 2015

ABSTRACT

In this report is described my Summer Student work in Fermilab. I worked in the Mu2e collaboration under the supervision of Dr P. Murat.
In Section 1 I briefly describe Mu2e experiment focusing on the experimental set up, the physical motivation and the the principal source of background.
In Section 2 I illustrate the calorimeter and the scintillation crystal that will be used in it, focusing on the kinetic of the crystal itself. In the last section I describe the different method used during the Summer Student Program to evaluate the kinetics of the crystal from data taken at Laboratori Nazionali di Frascati and preliminary results.

Fermilab

CONTENTS

LIST OF FIGURES

LIST OF TABLES

1 MU2E EXPERIMENT

[1] [2] [3]

Mu2e experiment purpose is the measurement of the ratio of rate of the neutrinoless coherent conversion of muon into electrons in the field of a nucleus normalized to the rate of muon capture on nucleus

$$R_{\mu e} = \frac{\Gamma\left(\mu^- + A(Z,N) \to e^- + A(Z,N)\right)}{\Gamma\left(\mu^- + A(Z,N) \to \nu_\mu + A(Z-1,N)\right)} \tag{1}$$

The experimental signature is a mono-energetic electron with an energy similar to the muon rest mass; this process is allowed in the Standard Model through neutrino oscillation but at the level of 10^{-54} so any signal is an evidence for physics beyond the SM.

1.1 Physics motivation

Observing the conversion process would be an evidence of Charged Lepton Flavour Violation processes, which have never been observed experimentally. It's important to underline that the rate at which CLFV occurs is model-dependent: experiments looking for CLFV events have to be sensitive to different processes in order to elucidate the mechanism responsible for flavour-violating effects. The most stringent limits currently come from the muon sector because of the high muon production rate and the long muon life time. The studied rare muons decays are:

- $\mu^+ \to e^+\gamma$
- $\mu^+ \to e^+e^+e^-$
- $\mu^-N \to e^-N$

In Table 1 are listed upper limits of CLFV processes

$BR(\mu^+ \to e^+\gamma)$	$< 5.7x10^{-13}$
$BR(\mu^\pm \to e^\pm e^+ e^-)$	$< 1.0x10^{-12}$
$BR(\mu^\pm \to \gamma\gamma)$	$< 7.2x10^{-11}$
$R\ (\mu^- Ti \to e^- Ti)$	$< 1.7x10^{-12}$
$R\ (\mu^- Au \to e^- Au)$	$< 7x10^{-13}$

Table 1: Data from current experimental limits at 90 % c.l.

While the observation of this process would be a major discovery and an evidence of CLFV, that allow the conversion far beyond what is expected from current standard theory, a non-observation would be equally interesting as it would place stringent limits on theory and exclude large regions of parameter space for leading theories of beyond-SM physics.

1.2 Experimental setup

The layout for the muon beam line and the detector system shows a typical S-shape: the entire system is surrounded by the Superconducting Solenoid Magnet System (Fig. 1)

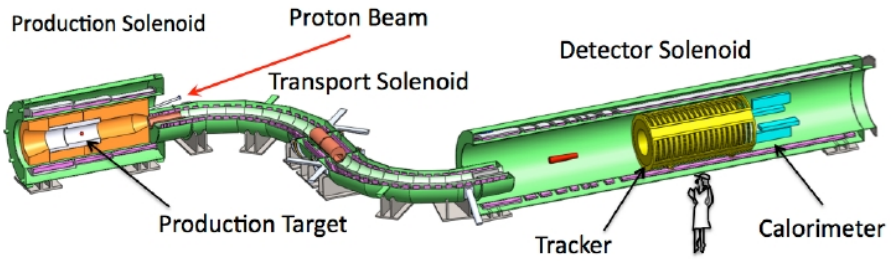

Figure 1: Schematic layout of the experimental apparatus

In order to limit backgrounds from muons that might stop on gas atoms and to reduce the contribution of multiple scattering for low momentum particles the solenoids has on internal pressure of 10^{-4} Torr The solenoids can be divided into 3 units that will operate as a single:

- **Production Solenoid (PS)**: high field magnet with a graded solenoidal field from 4.6 Tesla to 2.5 Tesla. PS captures pions and muons coming from decays and guides them toward the Transport Solenoid.
- **Transport Solenoid (TS)**: set of superconducting solenoids and toroids that form a magnetic channel that transmits low energy negatively charged muons from the Production Solenoid to the Detector Solenoid. Presence of absorbers and collimators along the TS stops negatively charged particles with high energy, positively charged particles and line-of-sight neutral particles. TS consists of five distinct regions: a 1 m long straight section, a 90° curved section, a second straight section about 2 m long, a second 90° curved section that brings the beam back to its original direction, and a third straight section of 1 m length.

- **Detector Solenoid (DS)**: large, low field magnet that houses the muon stopping target and the components required to identify and analyze conversion electrons from the stopping target. The muon stopping target resides in a graded field that varies from 2 Tesla to 1 Tesla. The graded field captures conversion electrons that are emitted in the direction opposite the detector components causing them to reflect back towards the detector.

The 8 GeV proton beam hit the target in the PS and back scattered negative particles are guided in the TS. The three TS's regions suppress particles with high momentum or positive charge and are long enough to allow the decay of almost all hadrons. The resulting muon's beam enters the Detector Solenoid and hits an aluminium stopping target: the muons can then be captured by the atoms and decay or convert into electrons, whose momentum and energy are measured by the cylindrical-shaped tracker and the two-disk calorimeter, respectively.

1.3 Signal and Predominant background

Mu2e experiment will search for process $\mu^- + N \rightarrow e^- + N$, where N is a nucleus of atomic mass A and atomic number Z. The conversion of a muon to an electron in the field of a nucleus is coherent: the muon recoils off the entire nucleus and the kinematics are those of two-body decay. Seen that the mass of a nucleus is large compared to the electron mass the recoil terms are small. A conversion electron is therefore monoenergetic with energy slightly less than the muon rest mass. The muon energy of 105.6 MeV is well above the maximum energy of the electron from muon decay at 52.8 MeV; hence, the vast majority of muon decays do not contribute to background. When a negatively charged muon stops in a target it rapidly cascades down to the 1S state. Capture, decay or conversion of the muon takes place with a mean lifetime that has been measured in various materials and ranges from less than $\sim$ 100 ns (high-Z nuclei) to over 2µs (low-Z nuclei). Depending of the target nucleus electron energy will be slightly less than the rest mass of the muon, as shown in 2

$$E_{\mu e} = m_\mu c^2 - E_b - \frac{E_\mu^2}{2m_N} \tag{2}$$

where m_μ is the muon mass, $E_b = Z^2\alpha^2 m_\mu/2$ is the atomic binding energy of the muon and last term is from nuclear re-

coil energy. The energy of the converted electron is $E_{\mu e} = 104.97$

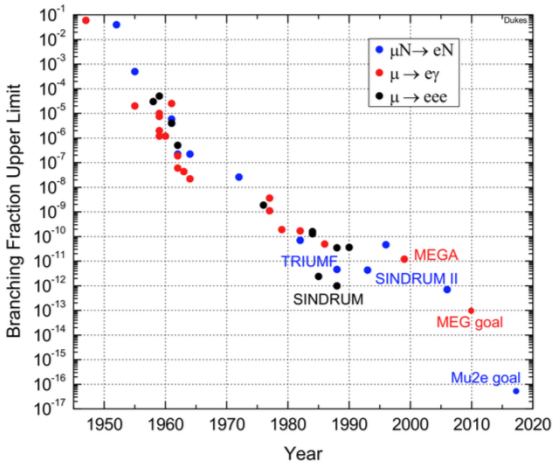

Figure 2: History of CLFV experiments

MeV for Al (Z = 13), which was selected mainly for the muon lifetime $\tau = 864$ ns in capture events, time interval that matches nicely the need of prompt separation in the Mu2e beam structure.Mu2e goal is to reach sensitivity of $10^{-16} - 10^{-17}$ on $R_{\mu e}(Al)$ which is more than four order of magnitude beyond the current limit as shown in figure 2.
At this this value of sensitivity there are several processes that simulate the muon to electron conversion signal, such as:

- **Muon Decay-In-Orbit (D.I.O.)**: if the muon is bound in atomic orbit an electron produced in the decay can exchange momentum with the nucleus. A small probability to have an electron with a maximum possible energy equal to that of a conversion electron exists.

- **Radiative Muon Capture (R.M.C.)** $\mu^- Al \to \gamma\nu Mg$: intrinsic source of high energy photons that can convert to an electron-positron pair in the stopping target or other surrounding material, producing an electron near the conversion electron energy. To reduce this background the stopping target is chosen so that the minimum masses of daughter nuclei are all at least a couple of MeV/c^2 above the rest mass of the stopping target nucleus, in order to push the RMC photon energy below the conversion electron energy.

- **Presence of antiprotons**: they can be coincident in time with a conversion electron, simulating the energy of a con-

version electron signal. The products of their interaction with the matter can be also a source of background.

- **Radiative pion capture**: pions can produce background through the capture by the nucleus: $\pi^- + N \rightarrow \gamma N^*$ because the kinetic endpoint has a peak at $\sim$ 110MeV and also because producted photons convert in pairs. This kind of background can be reduced with an appropriate signal time window.

- **presence of cosmic rays (electrons, photons, muons)**: potential source of electrons near the conversion electron energy. If such electrons have trajectories that appear to originate in the stopping target they can fake a muon conversion. Massive shielding and veto counters around the spectrometer and particle identification help to suppress this background electron

- **misreconstructed events**: to avoid this source of background it result fundamental to reduce high momentum resolution tails.

2 CALORIMETER AND CRYSTAL OVERVIEW

2.1 Calorimeter requirements and geometry

[3] [4]
The calorimeter must provide energy, position and timing information in order to confirm the events reconstructed by the tracker and distinguish fakes produced by cosmic rays and antiprotons.

The calorimeter should also be fast enough to provide a trigger for the experiment: the requirements of the electromagnetic calorimeter drive the choice of the scintillating material and in order to achieve the required energy and time resolution a total absorption homogeneous calorimeter is needed: the scintillating material must then have high light output (energy resolution), small Moliere radius (position resolution), fast scintillation decay time (to avoid pile-up) and good radiation hardness. The calorimeter final design [4] consists of two disks, positioned at a distance of half converted electron wavelength, with 674 CsI crystals.

Each crystal is readout by two large area 14x20 mm^2 UV ex-

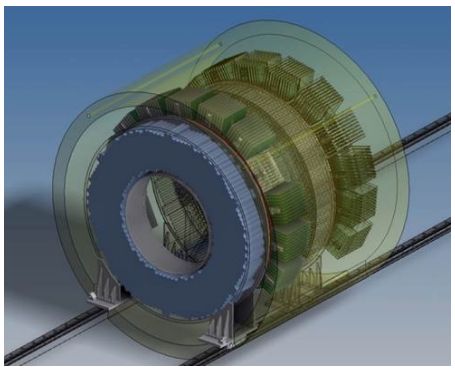

Figure 3: Calorimeter Design

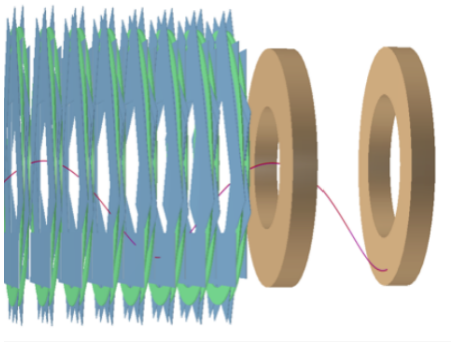

Figure 4: Side view of tracker and calorimetr

tended SIPM's and the analog front end electronics and digital electronics are located in the electronics' crates around the crystals.

2.2 Undoped Caesium Iodide

[5] [6] [7]
The crystal selected for the Mu2e experiment is the Caesium Iodide (CsI); single 34x34x200 mm^3 undoped, or pure, crystals will be used, with high γ-ray stopping power due to their relative high density and atomic number.
The CsI has an emission maximum at 315 nm, with an intensity one tenth that of the doped CsI crystals, and a small slow component.

The scintillation emissions properties are highly affected by the presence of trace impurities in quantities below ppm in the crystal and by growth process and the light output is heavily quenched at room temperature and, as show in figure 6, the decay curve's shape varies at different temperatures.

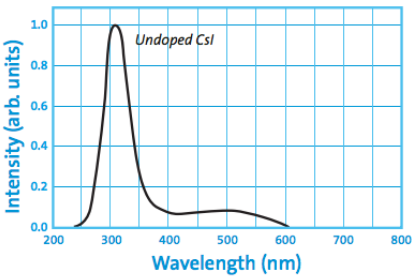

Figure 5: Scintillation emission spectrum of pure CsI[6]

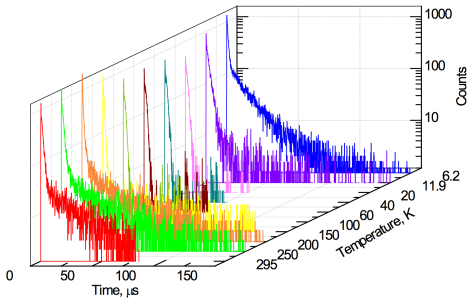

Figure 6: Isometric plot of decay curves of CsI measured for α-particle excitation (^{241}Am) at different temperatures.[7]

3 KINETICS OF THE CAESIUM IODIDE

[5] [8]
The kinetics of the crystal affects different aspects of the experiment, like for example, using a realistic shape of the crystal light emission in the Montecarlo give more accurate performance parameters of calorimeter as a result of the Montecarlo itself, or knowing how much long the slow component is can give a more realistic idea of the potential pile up or data volume expected in output of the FEE.
Different studies of the CsI have been made and focusing on the decay times of the emission we can find disagreement in old publication: one fast component with $\tau_F \sim 20$ ns, as shown in figure 7, or two different fast components with $\tau_{F1} \sim 6$ ns and $\tau_{F2} \sim 30$ ns, as shown in figure 8, and a slow component, highly depending on contamination and grow process, with a τ_S value spread around ~ 1 μs. Pure CsI samples from different producers for the Mu2e calorimeter have been analyzed by both Mu2e group of Caltech and Mu2e group of LNF for a characterize this different samples, of which ten are shown

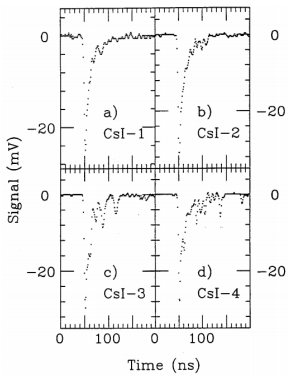

Sample	F (%)	τ_F (ns)	S (%)	τ_S (ns)
CsI-1	33	6.1±1.2	67	30±8
CsI-2	29	6.6±1.7	71	27±5
CsI-3	22	7.2±1.0	78	41±6
CsI-4	27	6.8±1.1	73	43±6

Figure 7: Decay spectra and times of pure CsI[5]

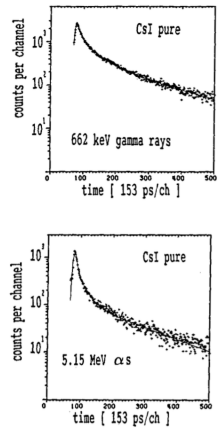

Fig.2. Decay spectra of undoped CsI.

Table II.
Decay times of undoped CsI.

662 keV gamma-rays		5.15 MeV alpha particles
21.7 ± 1.8 ns (65 %)	fast	20.6 ± 1.3 ns (50 %)
2.1 ± 0.2 ns (35 %)		2.2 ± 0.2 ns (50 %)
1.0 μs (50 %)	slow	0.1 μs (100 %)
0.1 μs (50 %)		

Figure 8: Decay spectra and times of pure CsI[8]

in figure 9, but data taking followed different procedure and instrumentation are here summarized.

Figure 9: Ten samples from three producers

3.1 Caltech

[9]
Crystals have been analyzed by the Caltech group using a Hamamatsu R2059 PMT with coincidence triggers from a ^{22}Na source and all samples were wrapped with two layers of Tyvek paper with precision and reproducibility of <1%.

Integrated charge is measured in bins of 50 ns in a 4000 ns interval, example shown in figure 10, and then fitted with the function

$$A_0 + A_1(1 - e^{-t/\tau_1}) + A_2(1 - e^{-t/\tau_2})$$

Ten different samples from three producers have been ana-

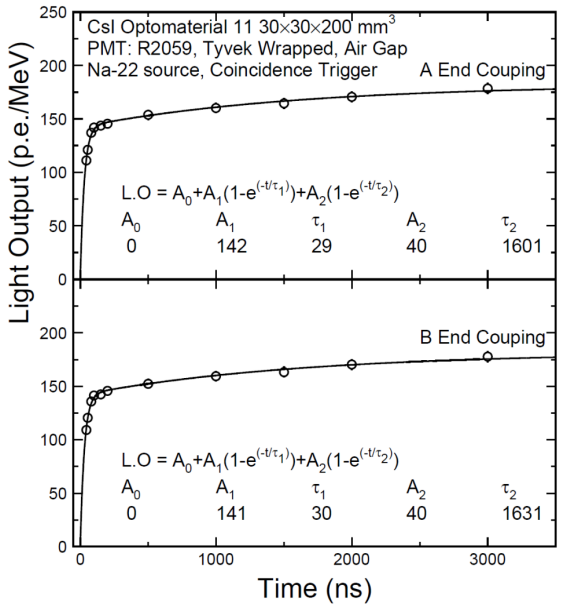

Figure 10: Charge integrated from the signal start to 4000 ns for a OPTOMATERIALS' crystal.

lyzed and results can be summarized:

- Fast component with $\tau_F \sim 30ns$, main contribution
- Slow component with $\tau_S \sim 1600ns$, contribution in some crystal is almost negligible

It's important to highlight that while the fast component is close to 30 ns the time bins are large 50 ns, this means that the fast component fit depends on few points.

3.2 LNF

[10]
This measurement has been carried out at the crystal station of Laboratori Nazionali di Frascati. The crystals, coupled to a UV extended PMT, are illuminated by a ^{22}Na source and the waveform of the digitized signals are integrated in steps of 20 ns from -30 to 900 ns around the peak pulse height.
For each crystal has been evaluated the fraction related to the

fast components as well as the decay time of both components and signal has been acquired with a CAEN DT5751 digitizer at 1Gsps.
So while Caltech group measured the integrated charge in time bins of 50 ns on a 4000 ns acquisition window the LNF group measured the waveform with 1 ns time bins on a 1000 ns acquisition window and then integrate the signal in 20 ns intervals and fit it with

$$p_0(1 - e^{-x/p_1}) + p_2(1 - e^{-x/p_3})$$

Sixteen different samples from three producers have been ana-

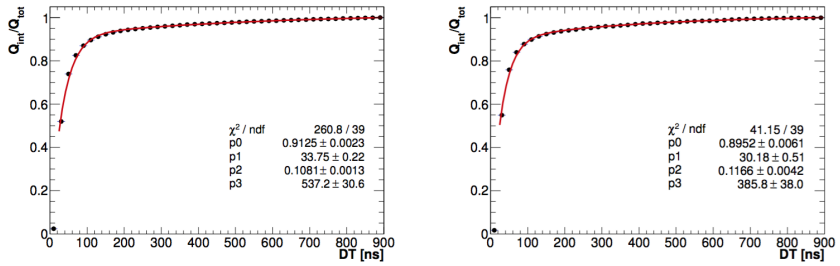

Figure 6: Ratio between the charge integrated from the signal start (DT = −30 ns), Q_{int}, and the total integrated charge, Q_{tot}, as a function of the DT variable for crystals from OPTOMATERIALS.

Figure 11: Ratio between the charge integrated from the signal star (DT = −30ns), Q_int, and the total integrated charge, Q_tot, as a function of the variable DT for OPTOMATERIALS' crystals.

lyzed and results can be summarized:

- Fast component with $\tau_F \sim 30ns$, main contribution
- Slow component with $500 \leqslant \tau_S \leqslant 1600$ ns

Some uncertainties could have been introduced in this procedure, especially using a running integral, which makes uncertainties on different points in figure 11 all correlated, and also align signal from different events, like the one in figure 12, using the higher bin can not be always the best option since noise can make that bin fluctuate. Also having a 1000 ns acquisition windows can affect fit results for the slow component.

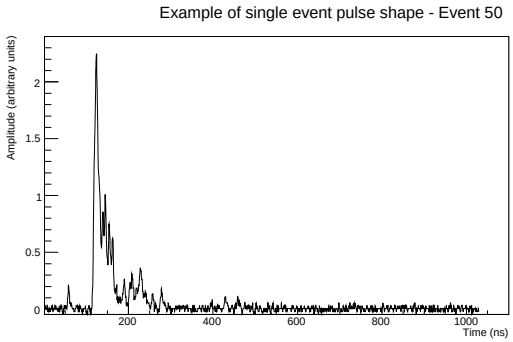

Figure 12: Example of single event pulse shape (Event number 50).

4 ANALYZING THE CSI PULSE SHAPE

The measurements of two different crystal has been considered in the following analysis

- Siccas CsI readout by an UV-extended PMT and tested with a ^{22}Na source (placed at different position w.r.t. the PMT on crystal longitudinal axis)
- ISMA CsI readout by PMT and tested with CRs

Measurements are part of the data taken and analyzed by the LNF group and data consists in count converted in volts, like the one in figure 12, and then the pedestal is subtracted.
The following analysis focus on finding a better way to evaluate how many components the undoped CsI has and their decay times from this measurements.
The first step is trying to reproduce the LNF group's results, that means integrating the charge of each event from 60 ns to 960 ns but instead of using integration intervals of 20 ns in this analysis the charge has been integrated in steps of 1 ns.
In this procedure, like in the one already followed by the LNF group, align all the signal before integration using the higher bin but integrate also the leading edge: this introduce a systematic error in value of the charge, so the same analysis has been carried out integrating from the highest bin to 800 ns later with the same integration step of 1 ns. Both results are showed in figure 13.

In both cases was not considered that every point uncertainty is correlated with all the other uncertainties; in order to avoid this we must avoid the running integral and fit directly the pulses' shape after normalizing and aligning all the

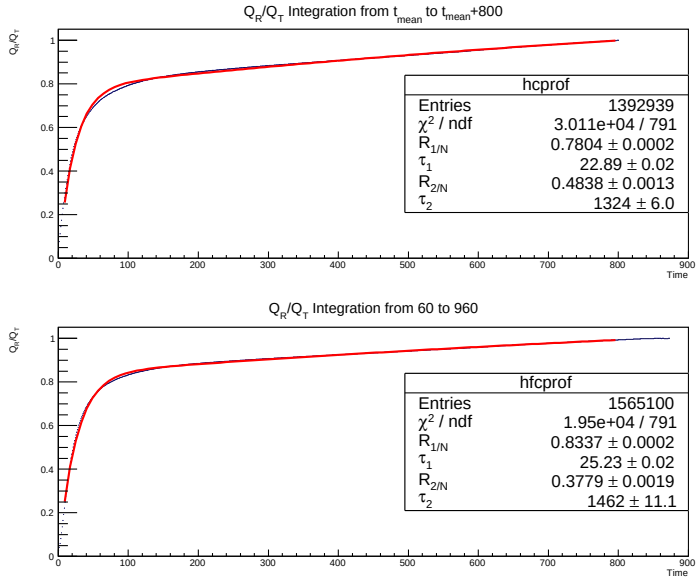

Figure 13: Running charge integral normalized to the overall charge with fit.

events using more accurate methods. Figure 14 shows a two-dimensional histogram filled with all the events and it's clear that both normalization and alignment are needed in order to obtain an average pulse shape.

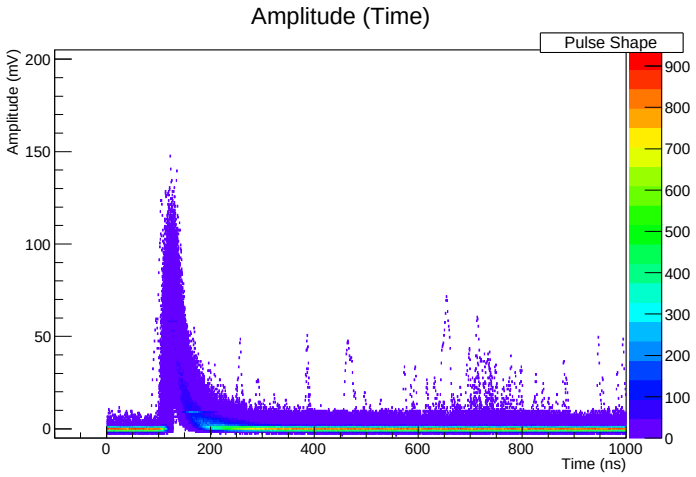

Figure 14: Two dimensional histogram filled with all events' pulse shape showing a spread on the alignment and height.

Before proceeding with the normalization and after looking different single event's pulse shape, example shown in figure **??**, we assume:

- All waveforms have the same shape

- All waveforms have the same rise time

cc With this assumption the next step is evaluating the

- Normalize the area to the integral
- Evaluate if another pedestal evaluation is needed
- Align all the pulse shapes using the slope of the leading edge

For each steps a two dimensional histogram similar to the one in figure 14 is filled with the new data. In the first step every bin is divided by the full integral of the pulse shape itself. After normalizing it is clear that the pedestal was not subtracted properly in all the events since some of them are above zero and some under zero in the previous plot so another pedestal is now evaluated with the first 50 ns where no peak can be found. The assumption that all waveforms have the same rise time means that we can evaluate the slope of the leading edge, fitting it with a straight line as shown in figure 17, and use the time bin of an arbitrary fixed point within the fit range to align all the events. The histogram obtained after this steps clearly shows that signals are aligned, the leading edge in figure 18 is narrower than the one in figure 14, and now it is possible to make out from the last histogram an "average" pulse shape which will be used for the fits.
Since there is still noise inside the data the average will be made projecting the histogram 18 in slices of 10 ns and taking the Gaussian mean of this distribution, examples in figure 19a as

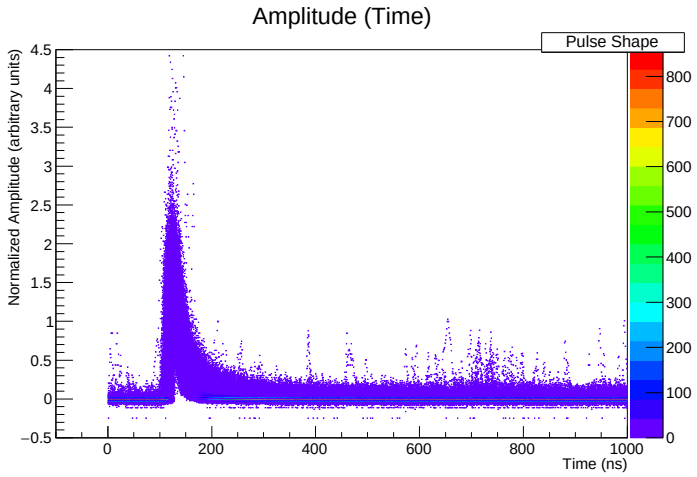

Figure 15: Two dimensional histogram after integral normalization.

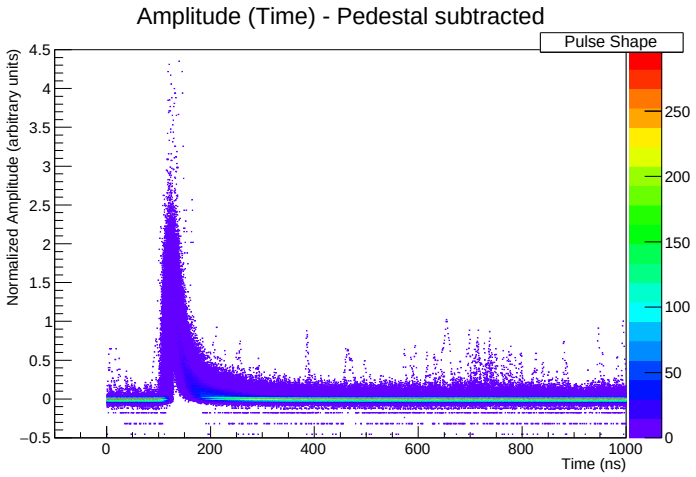

Figure 16: Two dimensional histogram after the subtraction of a new pedestal evaluated from the first 50 ns.

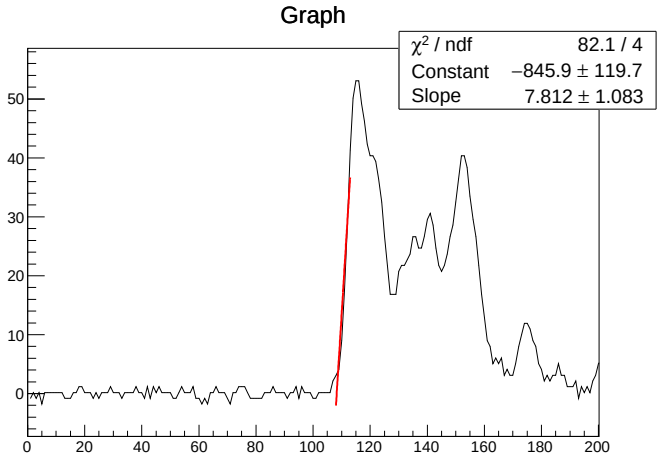

Figure 17: Example of single event pulse shape with a fit on the leading edge slope.

the point of the new plot.
To exclude the tails of the slices distributions and check if the results is independent from the range in which we do the Gaussian fit analysis has been repeated with a cut that prevent fitting the tails too; both the full range fit and excluded-tail fit are shown in figure 19.

Last step consist in plotting this points and fitting the components in order to obtain the decay times. It is clear from the averaged plot that only two component are present in this crystal and that between the beginning of the exponential tale, right after the peak, and the end of the tale itself there is a transition region in which behaviour is not due at only one component.

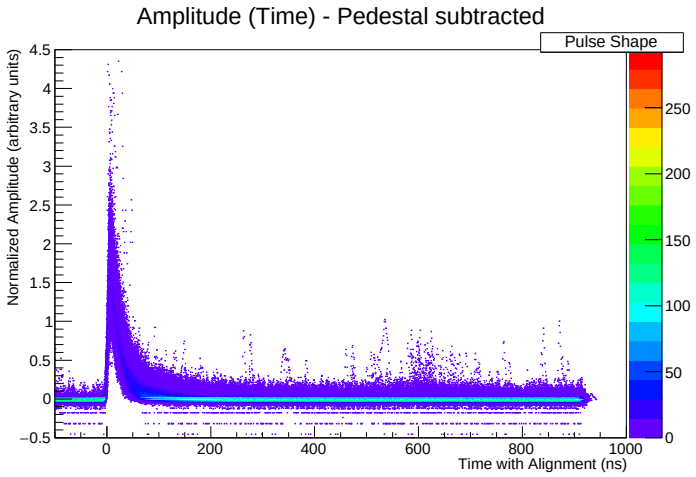

Figure 18: Two dimensional histogram after normalization and alignment.

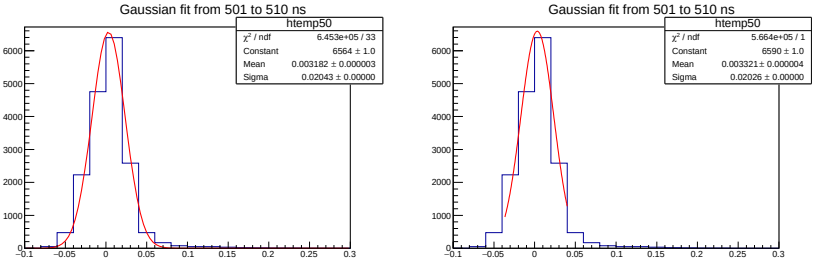

(a) Tales included. **(b)** Tales excluded.

Figure 19: Examples of Gaussians fit of a projected 10 ns slice.

This facts leads to the choice of fitting the two expected component separately in their range.
This procedure was repeated for the Siccas crystal tested with the source at different distances from the PMT and for the ISMA crystal tested with rays; plots and a summary table with all the results follows.

In the case of the ISMA crystal the distribution of the slices projected from the two dimensional histogram are more asymmetric, as shown in figure 19, this will worsen the accuracy of the Gaussian fit and will reflects in bigger uncertainties as shown in figure 24.

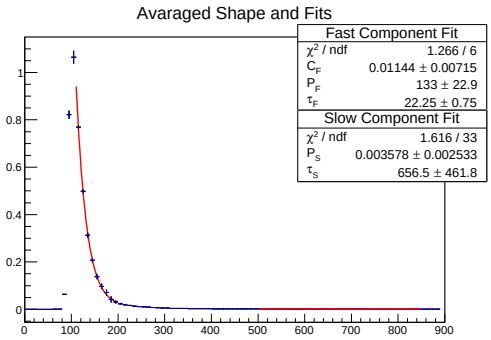

(a) Gaussian fit including tails.

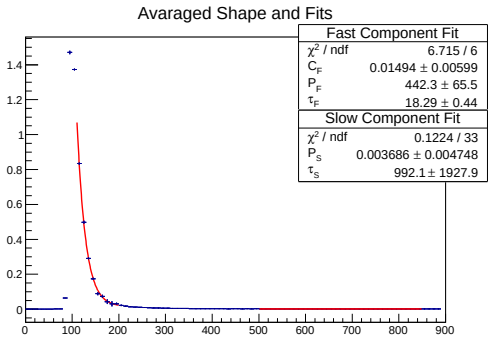

(b) Gaussian fit excluding tails.

Figure 20: Siccas 13 crystal, ^{22}Na source 2 cm from PMT, Tyvek wrapping.

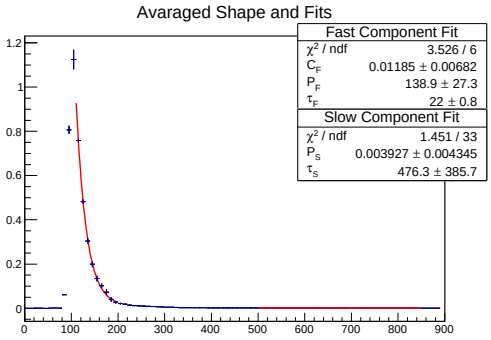

(a) Gaussian fit including tails.

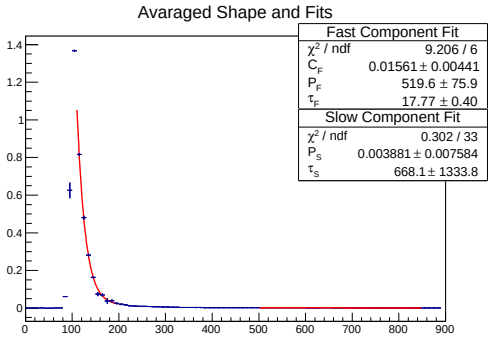

(b) Gaussian fit excluding tails.

Figure 21: Siccas 13 crystal, ^{22}Na source 10 cm from PMT, Tyvek wrapping.

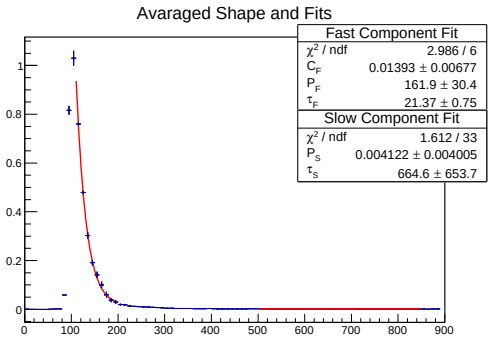

(a) Gaussian fit including tails.

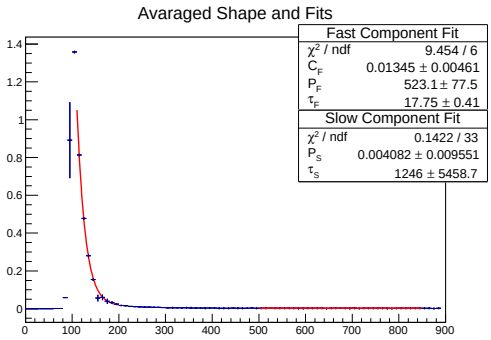

(b) Gaussian fit excluding tails.

Figure 22: Siccas 13 crystal, ^{22}Na source 16 cm from PMT, Tyvek wrapping.

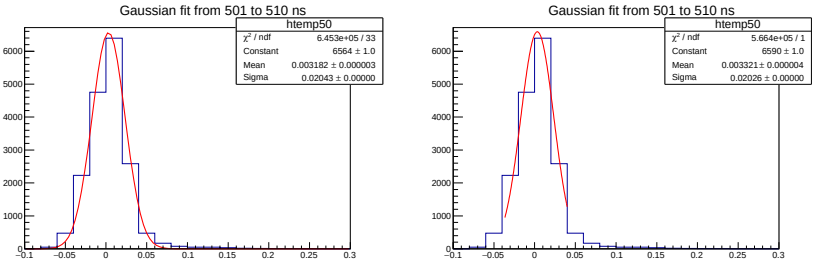

(a) Tales included. **(b)** Tales excluded.

Figure 23: Examples of Gaussians fit of a projected 10 ns slice.

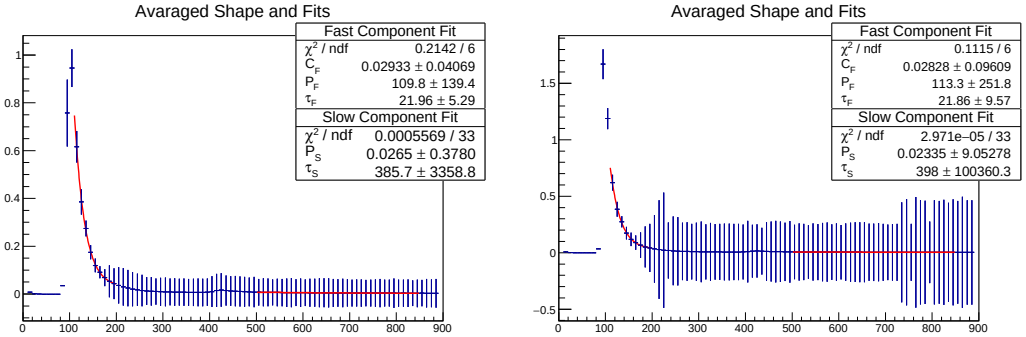

(a) Gaussian fit including tails. **(b)** Gaussian fit excluding tails.

Figure 24: ISMA crystal, cosmic rays and PMT, Tyvek wrapping.

Siccas Crystal	Source 2 cm from PMT, Gaussian Fit with tales
$\tau_F(ns)$	22.25 ± 0.75
$\tau_S(ns)$	656.5 ± 461.8
Siccas Crystal	Source 10 cm from PMT, Gaussian Fit with tales
$\tau_F(ns)$	22 ± 0.8
$\tau_S(ns)$	476.3 ± 385.7
Siccas Crystal	Source 16 cm from PMT, Gaussian Fit with tales
$\tau_F(ns)$	21.37 ± 0.75
$\tau_S(ns)$	664.6 ± 653.7
ISMA Crystal	Cosmic Rays, Gaussian Fit with tales
$\tau_F(ns)$	21.96 ± 5.29
$\tau_S(ns)$	385.9 ± 3422.5
Siccas Crystal	Source 2 cm from PMT, Gaussian Fit without tales
$\tau_F(ns)$	18.29 ± 0.44
$\tau_S(ns)$	992.1 ± 1927.9
Siccas Crystal	Source 10 cm from PMT, Gaussian Fit without tales
$\tau_F(ns)$	17.77 ± 0.40
$\tau_S(ns)$	668.1 ± 1333.8
Siccas Crystal	Source 16 cm from PMT, Gaussian Fit without tales
$\tau_F(ns)$	17.75 ± 0.41
$\tau_S(ns)$	1246 ± 5458.7
ISMA Crystal	Cosmic Rays, Gaussian Fit without tales
$\tau_F(ns)$	21.86 ± 9.57
$\tau_S(ns)$	398 ± 100360.3

5 CONCLUSION

Studying the kinetics of the Caesium Iodide and analyzing the data from two different samples, tested with different sources, led to the conclusion that there is no evidence of a component with decay time close to ~ 6 ns.
The fit of the pulse shape shows a fast component with decay time τ_F ~ 20 ns, consistent with some old publication but lower then the result of the fit on the integrated charge.
The decay time of the slow component is spread between ~ 380 ns and ~ 1200 n, lower then the result of the fit on the integrated charge, but less reliable then τ_F because of the asymmetric distribution fitted with a Gaussiann.
This procedure can still be improved and after getting adequately accurate decay times, a double exponential, to describe the tale analyzed in this work, can be convoluted with a function describing the readout electronics; this convolution will be a realistic output of the calorimeter electronics and can be used in the Montecarlo.

REFERENCES

[1] Mu2e Collaboration. Mu2e Technical Design Report. *Fermi National Accelerator Laboratory*, 2014

[2] R. Bernstein, P.S. Cooper. Charged lepton flavour violation: An experimenter's guide. *Fermi National Accelerator Laboratory*, 2013

[3] R. Soleti. Study of requirements and performances of the electromagnetic calorimeter for the Mu2e experiment at Fermilab. *Mu2eDocDB 5130*, 2015

[4] S. Miscetti. Calorimeter Final Design Review: Overview of the Mu2e Calorimeter. *Mu2eDocDB 6708-v9*, 2016

[5] Z. Wei, R. Zhu. A study on undoped CsI crystals. *Nuclear Instruments and Methods in Physics Research A326 (508-512)*, 1993

[6] Saint-Gobain Ceramics & Plastics. CsI Pure Data Sheet. *www.crystals.saint-gobain.com*, 2014

[7] V.B. Mikhailik, V. Kapustyanyk, V. Tsybulskyi, V. Rudyk, H. Kraus. Luminescence and scintillation properties of CsI: A potential cryogenic scintillator. *Physica Status Solidi B-Basic Solid State Physics 252, (804-810)*, 2015

[8] P. Schotanus, R. Kamermans. Scintillation characteristics of pure and Tl-doped CsI crystals. *IEEE Transactions on Nuclear Science 37 (177-182)*, 1990

[9] R.Zhu. Status of CsI crystals for DOE CD3c Review. *Mu2eDocDB 7533-v5*,2016

[10] M. Cordelli, R. Donghia, S. Giovannella, S. Miscetti, I. Sarra. Measurement of the slow component for undoped CsI crystals. *Mu2eDocDB 6813-v2*,2016